

# MERLIN radio detection of an interaction zone within a binary Orion proplyd system.

M. F. Graham, J. Meaburn, S. T. Garrington and T. J. O'Brien

*Jodrell Bank Observatory, University of Manchester, Macclesfield, Cheshire, SK11 9DL, UK*

[mgraham@ast.man.ac.uk](mailto:mgraham@ast.man.ac.uk)

W. J. Henney

*Instituto de Astronomía, Universidad Nacional Autónoma de México, Campus Morelia, Apartado Postal 3-72 (Xangari), 58089 Morelia, Michoacán, México*

C. R. O'Dell

*Department of Physics and Astronomy, Box 1807-B, Vanderbilt University, Nashville, TN 37235*

## ABSTRACT

Presented here are high angular resolution MERLIN 5 GHz (6 cm) continuum observations of the binary proplyd system, LV 1 in the Orion nebula, which consists of proplyd 168–326SE and its binary proplyd companion 168–326NW (separation 0.4''). Accurate astrometric alignment allows a detailed comparison between these data and published *HST* PC H $\alpha$  and [O III] 5007 Å images.

Thermal radio sources coincide with the two proplyds and originate in the ionized photoevaporating flows seen in the optical emission lines. Flow velocities of  $\approx 50 \text{ km s}^{-1}$  from the ionized proplyd surfaces and  $\geq 100 \text{ km s}^{-1}$  from a possible micro-jet have been detected using the Manchester Echelle spectrometer.

A third radio source is found to coincide with a region of extended, high excitation, optical line emission that lies between the binary proplyds 168–326SE/326NW. This is modelled as a bowshock due to the collision of the photoevaporating flows from the two proplyds. Both a thermal and a non-thermal origin for the radio emission in this collision zone are considered.

## 1. Introduction

It is now well established that the compact, highly ionized gaseous knots (LV 1-6) near the Trapezium stars in M42, discovered by Laques & Vidal (1979) contain young low

mass stars (YSOs) still partially cocooned in their primaeval material. See Figure 1 for their locations. Many similar objects were found in the same vicinity at radio wavelengths (Churchwell et al. 1987; Garay 1987; Garay, Moran, & Reid 1987; Felli et al. 1993a; Felli et al. 1993b). The LV knots are particularly interesting both because of their close proximity to the Sun, permitting detailed observation, and because of their extreme local environment. This environment is swept by the energetic particle wind of the nearby O6 star,  $\theta^1$ Ori C and the LV knots are irradiated by its Lyman (and near UV) photons. Their outside surfaces are consequently highly ionized, though shielded from the direct wind from  $\theta^1$ Ori C by a standoff bowshock (Figure 3) in the photoevaporated flow.

*HST* imagery revealed the structure of these systems, now known as ‘proplyds’ (O’Dell, Wen, & Hu 1993), with startling clarity (O’Dell & Wong 1996; Bally et al. 1998). The central stars, found originally on a  $2\ \mu\text{m}$  IRACAM ‘engineering’ image with UKIRT by Meaburn (1988) and subsequently by McCaughrean & Stauffer (1994) are seen to be embedded in dense cocoons/disks of dusty molecular gas. Photoevaporated flows from the ionized surfaces form cometary tails pointing away from  $\theta^1$ Ori C as they meet the UV flux of this star. Supersonic flow velocities of  $\geq 50\ \text{km s}^{-1}$  were found (Meaburn 1988; Meaburn et al. 1993; Massey & Meaburn 1995) using the Manchester Echelle spectrometer (MES - Meaburn et al. 1984) on a variety of telescopes. The origin of these ionized flows has been modelled, initially as a two-wind interaction (Henney et al. 1996, 1997) and more recently as the interaction of the flow from the proplyd disk with the ionizing Lyman photon field of  $\theta^1$ Ori C and the nebula (Johnstone, Hollenbach, & Bally 1998; Henney & Arthur 1998; Henney & O’Dell 1999; Störzer & Hollenbach 1999). The two-wind interaction is now thought to manifest itself much further from the proplyd disk in the form of the standoff bowshocks (one of which is shown in Figures 1 and 3) observed by Hayward, Houck and Miles (1994), McCullough et al. (1995) and Bally et al. (1998). The flow from the proplyd itself is most likely caused by photoevaporation of the disk by either ionizing (EUV) or non-ionizing (FUV) photons from  $\theta^1$ Ori C, depending on the proplyd’s proximity to it (Johnstone, Hollenbach, & Bally 1998). The process of photoevaporation, photoionization, and acceleration of the disk gas down the surrounding density gradient is found to produce flow velocities of only 2-3 times the sound speed of  $\sim 10\ \text{km s}^{-1}$  (Dyson 1968), which does not fully account for the velocities observed in the longslit spectra. These longslit spectra were complemented by the Fabry-Perot work of O’Dell et al. (1997), which compared velocity data with *HST* images and suggested the presence of a micro-jet associated with one of the proplyds.

The presence of predominantly monopolar jets from the YSOs in many of these proplyds was first suggested by the  $\geq 100\ \text{km s}^{-1}$ , spatially compact ( $\leq 1$  arcsec across) spikes or knots on the MES position-velocity (pv) arrays of Meaburn et al. (1993) and Massey & Meaburn (1995). This has now been confirmed through direct *HST* imagery by Bally, O’Dell, &

McCaughrean (2000), who find more than 20 jets associated with various proplyds. This apparent ubiquity of jets and the fact that it is difficult to get high velocity flows from density gradients suggest that most collimated high velocity features are jets. *HST* imagery, as a consequence of its high angular resolution, along with high resolution near infra-red imagery (Petr 1998), has also revealed the binary nature of a small fraction of the proplyds.

The binary structure of the prominent proplyd originally designated LV 1 when unresolved in ground-based observations is of particular interest. It was first resolved into two sources in the 2 cm VLA A-array radio maps of Felli et al. (1993a) (Sources 5 and 20 in their Tables 2 and 3). The higher resolution *HST* image shows that this system is formed by two proplyds separated by  $0.4''$ , which are catalogued as 168–326N and as 168–326S, by O’Dell & Wen (1994). In the subsequent full catalogue of stars and compact objects of O’Dell & Wong (1996), it appears as a single proplyd, 168–326, corresponding to Felli et al.’s (1993a) source 20. However, the near infra-red  $0.13''$  resolution binary star survey of Petr (1998) identifies 168–326 as a binary system consisting of two components that are referred to as 168–326E and 168–326W. Bally et al. (1998), who used the same *HST* observations as used here, label the two components as 168–326 and 168–326a (their figure 2) and mention the presence of a bright arc lying between the sources. Here, the proplyds are referred to as 168–326SE and 168–326NW, which is the clearest form of designation. In the present paper the discovery is reported of the interaction zone between the flows from 168–326SE and 326NW in both the radio (at 5 GHz with MERLIN) and optical ( $\text{H}\alpha$  and  $[\text{O III}] 5007 \text{ \AA}$  with the *HST*) domains. The collision of two photoevaporated flows is explored to explain the nature of this interaction. Further kinematical and morphological evidence for a jet in LV 1 is also presented.

## 2. Observations

### 2.1. Imagery

#### 2.1.1. Radio

MERLIN observations of the Orion nebula were made between 1998 December 21 and 1999 February 15 at 5 GHz (6 cm) with a bandwidth of 15 MHz. The observations, taken over 8 days, alternated every 10 minutes between a phase calibrator, 0539-057 and the target itself. 3C286 was used to get a flux for a point source at the time of the observations. The phase calibrator was used in order to remove atmospheric density variations from the target source data and also to register the astrometric alignment of the images to an accuracy approximately  $0.010''$ . Initial data editing and amplitude calibration were done using the

MERLIN-specific d-programs. Subsequent phase calibration was then carried out in the National Radio Astronomy Observatories' (NRAO) AIPS package. The resulting data were CLEANed using the AIPS task IMAGR and finally restored with a circular beam of full width at half-maximum, FWHM = 0.080''. More details of the reduction of the radio data can be found in a parallel paper on LV 2 (Henney et al. 2001).

### 2.1.2. Optical

The optical observations presented here were obtained with the *HST*'s Planetary Camera (PC) under J. Bally's observing program, GO 5469. The images used were obtained at the target named NGC1976-LV3 through the F656N ( $\text{H}\alpha$ ) and F502N ( $[\text{O III}]$  5007 Å) filters. For each filter there were three images at this position, each lasting 60 s, for the  $\text{H}\alpha$  filter and 100 s for the  $[\text{O III}]$  5007 Å filter. In both cases, the three images were combined using the NOAO IRAF package's CRREJ routine, which removes cosmic rays during the combining process. The images were then rotated by an amount such that north was at the top of the image and east was at the left, using the image header keyword ORIENTAT, which gives the position angle of the y axis of the PC detector projected on the sky, in degrees east of north.

Images in the F658N and F547M filters were also used to make an exact flux calibration using the method of O'Dell and Doi (1999), which corrects for underlying continuum and contamination by adjacent lines.

### 2.1.3. Alignment of Radio and Optical Images

The process of phase referencing MERLIN images results in an absolute astrometric calibration that is accurate to approximately 0.010'' and tied to the radio reference frame (ICRF). However the absolute co-ordinate system that is built in to *HST* images is known to be inferior to this by an order of magnitude. Therefore, alignment of the optical and radio images was done by shifting the co-ordinate system of the optical images and taking the radio co-ordinate system to be correct. Ideally, the optical images could be re-calibrated empirically using stars in the field with *HIPPARCOS* positions, of which there are three. Unfortunately, these three stars,  $\theta^1\text{Ori A}$  (HIP 26220),  $\theta^1\text{Ori C}$  (HIP 26221), and  $\theta^1\text{Ori D}$  (HIP 26224) are badly saturated in the *HST* PC images, meaning that their positions on the PC CCD chip cannot be reliably determined.

In the vicinity of  $\theta^1\text{Ori C}$ , MERLIN clearly detected all six LV knots at 5 GHz. These six

proplyds are also obvious on the *HST* images (figure 2 of Bally et al. 1998). A comparison of the centroided optical and radio positions as given by their respective co-ordinate systems leads to a consistent difference between the two. As a result, this difference of a few hundred milliarcseconds was applied to the co-ordinate system of the *HST* images, in order to correct and align them with the MERLIN image. It is not unreasonable to expect that there is a real difference in the position of the optical and radio emission from these objects, which puts this method into question. However, this difference is likely to be a lot less than the gross error of a few hundred milliarcseconds in the *HST*’s astrometric calibration. Also, this real separation in optical and radio position would be expected to be along the line joining the proplyd to the ionizing source ( $\theta^1$ Ori C). Therefore, the fact that the five proplyds used for the alignment surround  $\theta^1$ Ori C and are oriented at various position angles means that the real difference is somewhat preserved. In effect, the difference in radio and optical positions has been minimised as opposed to removed. It should be noted that LV 6 was not used because its radio position was hard to determine, due to its apparently complicated structure.  $\theta^1$ Ori A is a strong radio source, but could not be used in the alignment as its radio position was found to be significantly displaced from its optical position. The final astrometric calibration was found to be consistent with that of Henney et al. (2001).

## 2.2. Echelle Spectroscopy

The Trapezium region of the Orion nebula, shown in Figure 1, has been explored spectroscopically with longslit spectra obtained with the MES (Meaburn 1988; Massey & Meaburn 1993; Meaburn et al. 1993; Massey & Meaburn 1995). The pv array of [O III] 5007 Å profiles shown in Figure 2 was taken at the slit position referred to as S1 in Massey & Meaburn (1995) with the MES on the 2.5m Isaac Newton Telescope. The slit position is shown in Figure 1 and the full observational setup for the data can be found in Massey & Meaburn (1995). Stellar continuum from  $\theta^1$ Ori C has now been subtracted from this spectrum, leaving some residual noise, but also allowing the emission from LV 1 to be more easily appreciated.

The emission from LV 1 is identified in Figure 2. It is most intense out to velocities of  $\pm 50$  km s $^{-1}$  with respect to the nebula and extends more faintly to  $\approx 100$  km s $^{-1}$  with respect to the systemic heliocentric radial velocity,  $V_{\text{sys}} = 25$  km s $^{-1}$ . Such a high speed ‘spike’ in the pv array is indicative of a jet and although one was not originally identified in the *HST* imagery of Bally, O’Dell, & McCaughrean (2000), García-Arredondo, Henney & Arthur (2001) present evidence of a micro-jet from 168-326SE at a position angle of +85°. This jet is shown in Figure 3 to be predominantly monopolar, although there is a hint of an approaching component in the PV array in Figure 2.

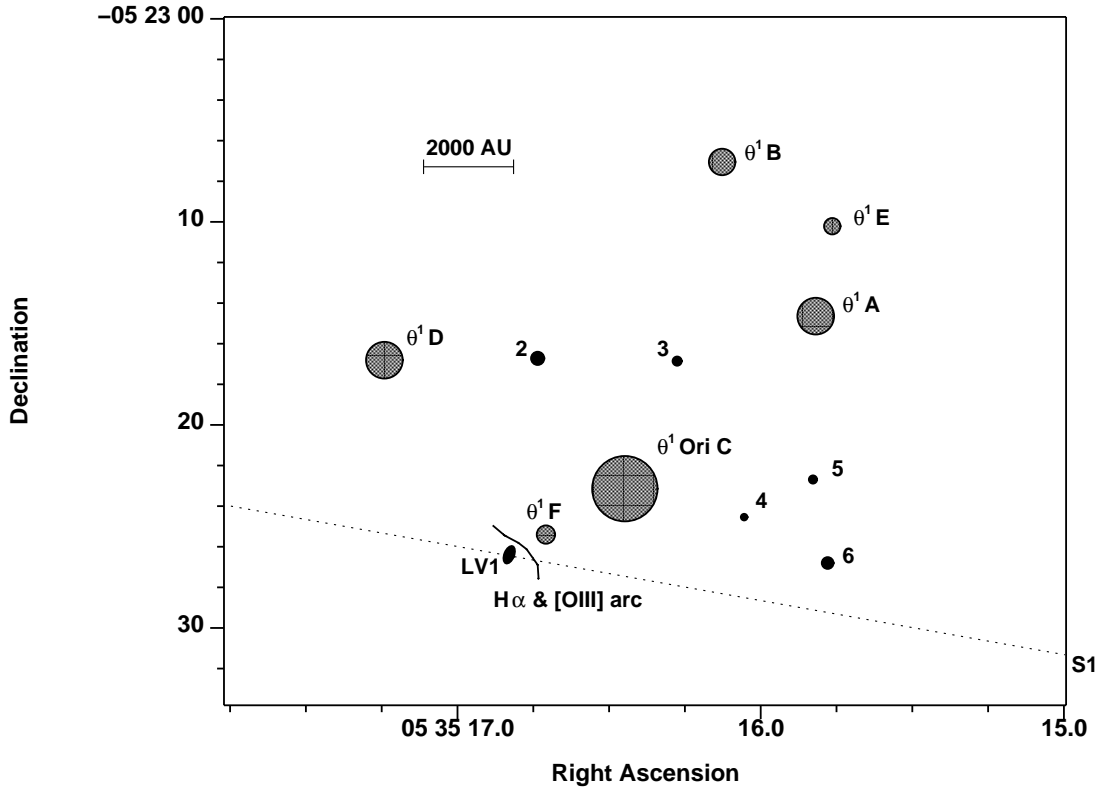


Fig. 1.— Identification chart for the Trapezium region. The  $\theta^1$ Ori stars are shown as grey circles and labelled with their  $\theta^1$ Ori designation. Proplyds are shown as black circles and are labelled with their LV number. LV 1 is shown as an ellipse to indicate its extended binary nature. The position of the arc/bow shock that shields the LV 1 binary system from the fast wind of  $\theta^1$ Ori C is also shown, along with the position of the MES slit, S1.

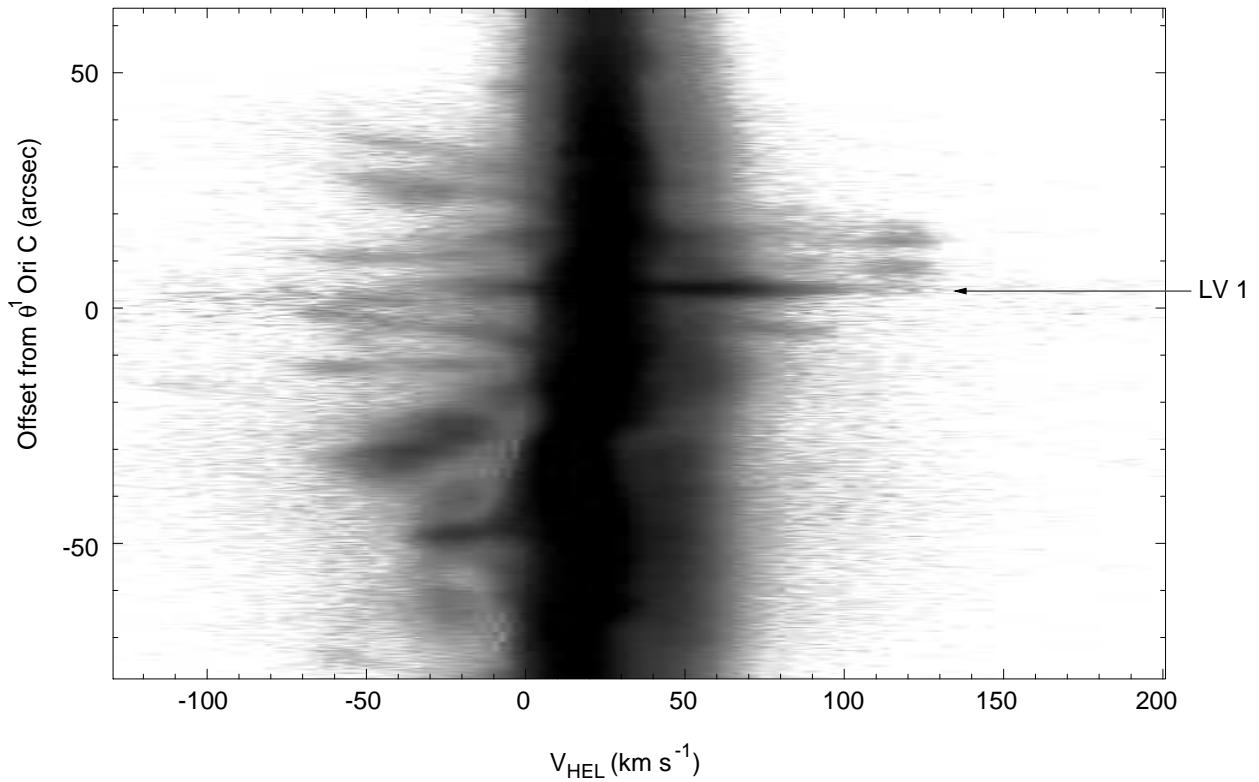


Fig. 2.— [O III] 5007 Å pv array of LV 1 taken with the Manchester echelle spectrometer at slit position S1. The position of LV 1 on this slit length is indicated. A positive offset is eastwards along the dotted line shown in Figure 1.

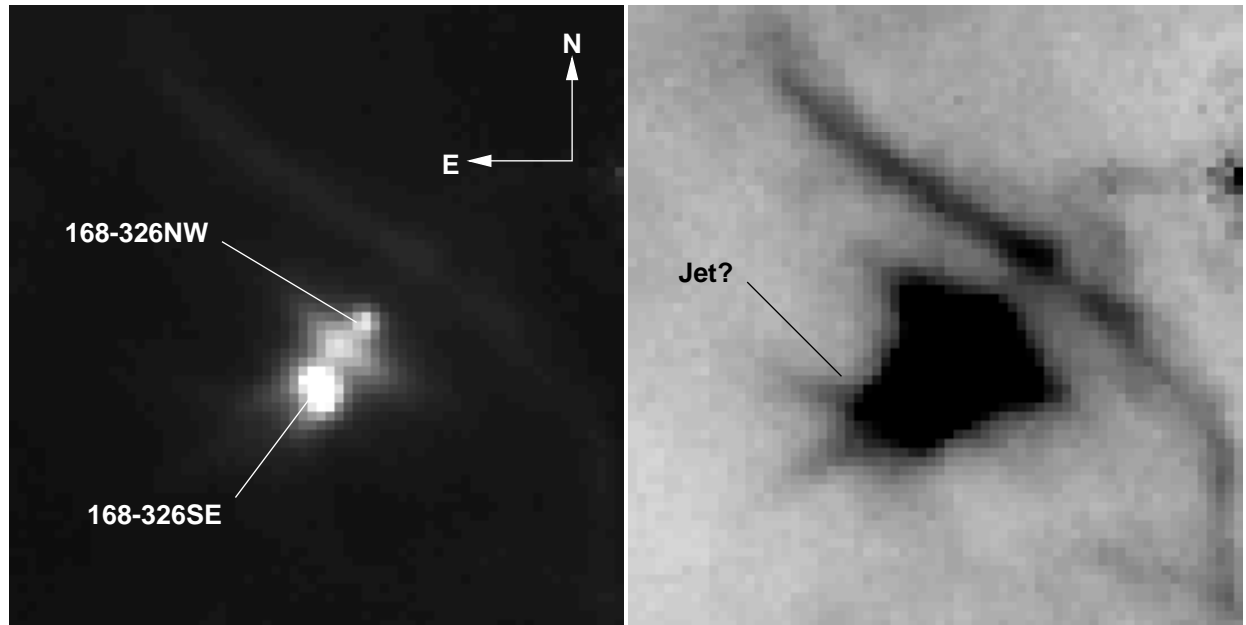


Fig. 3.— [O III] 5007 Å *HST* image of LV 1 now resolved into its binary proplyd components 168-326NW and SE. Left: Positive greyscale showing the individual binary components. Right: Negative greyscale at a different contrast to show fainter features, such as the proplyd flow-stellar wind interaction bowshock and the predominantly monopolar micro-jet with a PA of 85°.

### 3. Radio/Optical Comparisons

The identification chart for the Trapezium region in Figure 1 shows  $\theta^1$ Ori A-F, the six LV objects, and the bowshock that marks the interface between the low speed proplyd disk flow of LV 1 and the high speed stellar wind of  $\theta^1$ Ori C. This interaction shields the LV 1 binary system from a direct interaction with  $\theta^1$ Ori C’s wind and happens on a much larger scale than the interaction between the two proplyds which constitute LV 1 (168–326SE and 168–326NW).

Three distinct sources can be seen in the MERLIN 5 GHz radio contours shown in Figures 4 and 5, which compare the 5 GHz radio emission to the H $\alpha$  and [O III] 5007 Å emission respectively. The result of the alignment techniques described above is that the south-east radio source corresponds to 168–326SE and the north-west radio source corresponds to 168–326NW. This leads to the strong possibility that the radio source located between the binary components is the result of an interaction between them.

This interaction zone is not as prominent in the H $\alpha$  image. Furthermore, the peak radio to peak H $\alpha$  flux ratios for the two proplyds are the same, whereas this ratio for the interaction source is just over 2.56 times that for the proplyds. This could indicate that the interaction radio emission has a non-thermal origin (see Section 5).

However, the interaction zone can be seen in the light of the [O III] 5007 Å line, as shown in Figure 4. This could mean that the region has a temperature high enough (i.e.  $> 10^4$  K) to radiate predominantly in [OIII], as opposed to H $\alpha$ . A different density in this region compared with the proplyds, combined with this higher temperature could therefore generate sufficiently enhanced thermal radio emission (see § 5) to give the enhanced radio/H $\alpha$  ratio that is observed without invoking non-thermal radio processes.

The position of the brightest part of the interaction source in the [O III] 5007 Å image is of particular interest. In this image, the tail of 168–326SE can be seen pointing almost exactly away from  $\theta^1$ Ori C. This is a common feature of many of the proplyds (Bally et al. 1998) and leads to the conclusion that the diffuse photon flux of the nebula is causing a flow off the ‘back’ of the proplyds. The brightest point of the interaction source is on the opposite side of 168–326NW to  $\theta^1$ Ori C and not directly on the axis joining the two binary components. A simplistic explanation for this is that the interaction is happening between material flowing off the ‘back’ of 168–326NW into the flow from the ‘front’ of 168–326SE.

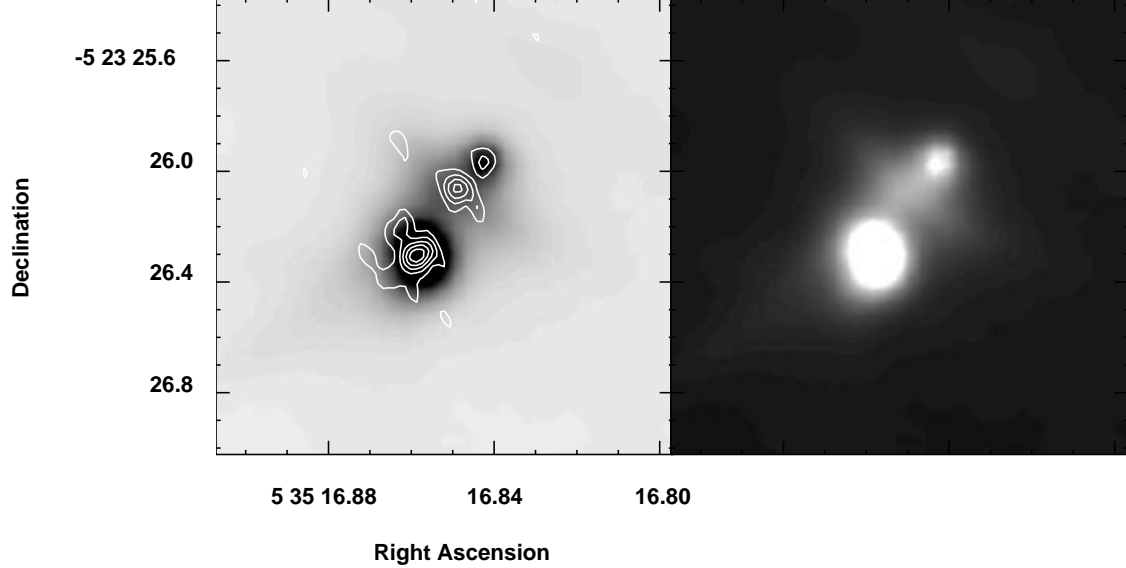


Fig. 4.— Left: MERLIN 5 GHz contours at  $4 \times 10^{-4} \times (1, 1.5, 2, 2.5, 3)$  Jy/BEAM superimposed on the negative greyscale *HST* H $\alpha$  (F656N) image of LV 1 (168–326SE and 326NW). Right: Greyscale *HST* H $\alpha$  (F656N) image of LV 1 (168–326SE and 326NW). Note that this field-of-view is about the size of the oval marked LV 1 in Figure 1.

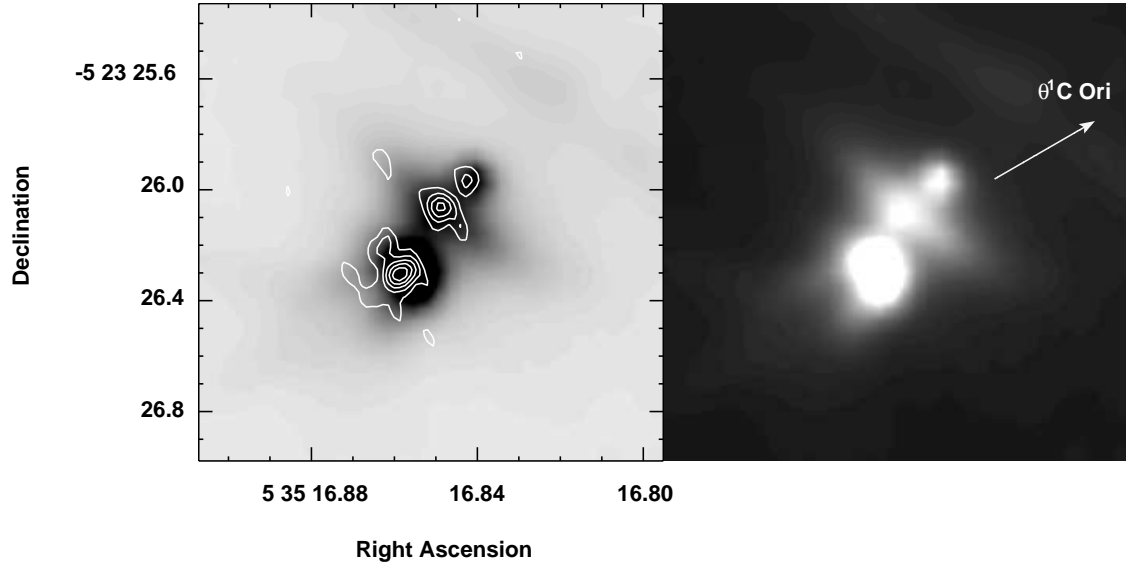


Fig. 5.— As Figure 4 but versus the [O III] 5007 Å (F502N) *HST* image, along with the direction of the ionizing star  $\theta^1$  Ori C.

#### 4. Modelling the Interaction

The morphology of the binary proplyd system, LV 1, shown in Figure 5 can be summarised as follows. There is a bright interaction peak of emission at 5 GHz between the two proplyds, which is nearer the smaller proplyd, 168–326NW. This peak is the brightest part of an arc of emission in H $\alpha$  and [O III] 5007 Å that is concave with respect to the smaller proplyd. The peak does not lie on the line connecting the two proplyd ‘heads’, but instead lies behind 168–326NW as seen from  $\theta^1$ Ori C. This morphology seems to represent the first evidence for a hydrodynamic interaction between two proplyds. A schematic model of such an interaction is shown in Figure 6, in which the transonic photoevaporated flows of a few 10’s of km s $^{-1}$  (as seen in Figure 2) from each proplyd’s disk, driven by the UV radiation from  $\theta^1$ Ori C, are colliding to form a dense interproplyd shell bounded by two weak shocks. The shell formed by the interaction of the disk flows from two proplyds with the stellar wind of  $\theta^1$ Ori C is also shown. Canto, Raga, & Wilkin (1996, hereafter CRW) have studied the interaction between two hypersonic, non-accelerating, spherical winds forming an axisymmetric bowshock structure under the approximation that the interaction region forms a thin, momentum-conserving shell. The situation with the proplyds is more complicated, mainly because the individual flows are non-isotropic, which will result in a totally asymmetric bowshock. However, the following principal results of the model appear to have observational counterparts in the LV 1 system:

1. There will exist a point, termed the *stagnation point*, where the shell surface is perpendicular to the velocity vectors of both flows. This forms the ‘nose’ of the bowshock and its position is determined by the condition of ram pressure balance; it will be closer to the less powerful proplyd in terms of wind momentum flux. The normal to the shell surface at the stagnation point can be considered the bowshock axis, even though it is not an axis of symmetry.
2. The shell will curve back towards the less powerful flow. At each azimuth around the bowshock axis, the shell will tend asymptotically to a constant opening angle from the axis, but the anisotropy of the flows will lead to this opening angle varying with azimuth.

The stagnation point is the area of highest density in the interaction shell and will therefore show up as a peak in the intensity of any bowshock that lies between the proplyds and is therefore clearly identifiable in Figure 5. The anisotropy of the flows means that the stagnation point need not necessarily lie on a line joining the proplyd heads. The observed radio emission at the stagnation point takes the approximate form of a point source, with some evidence of extension at  $PA \approx 45^\circ$  in the lowest ( $3\sigma$ ) contour level (Figures 4 & 5). If

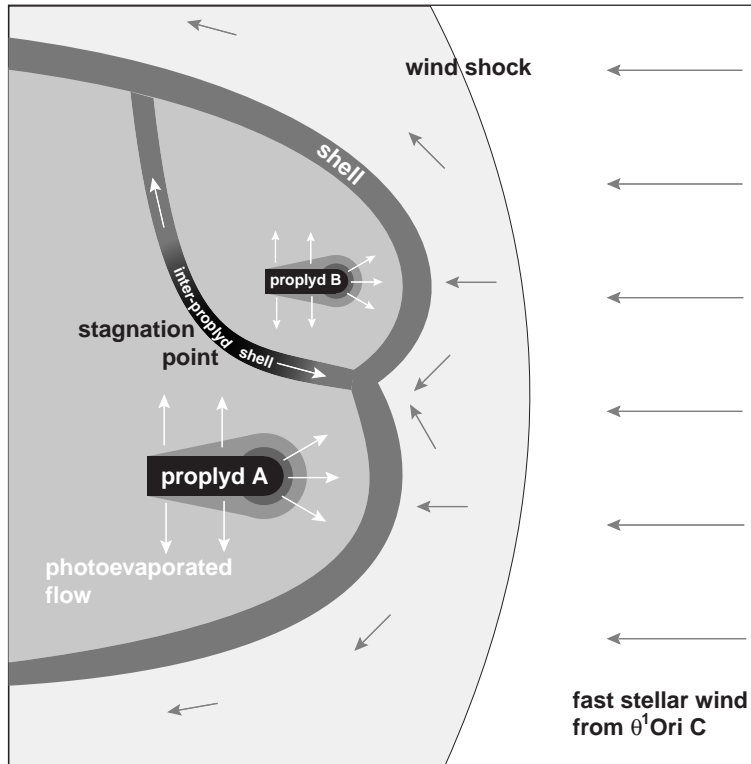


Fig. 6.— A schematic of the three-flow interaction that will occur when a binary proplyd system is found close to  $\theta^1$  Ori C, showing the plane containing the two proplyd major axes. In addition to the standoff shell between each proplyd and the stellar wind, there is also an interproplyd shell.

the radio emission does continue to extend in the same way as the optical, it could be below the sensitivity of these observations.

The details of deciphering the geometry of the interacting binary system and then applying the model of CRW is left to a subsequent paper (Henney 2001). However, a preliminary result of considering the 3-dimensional geometry of LV 1 leads to two possible geometrical configurations for the system, as shown in Figure 7. Both configurations imply that the proplyds lie approximately between the observer and  $\theta^1\text{Ori C}$ , i.e. the observer is ‘behind’ the proplyds with respect to  $\theta^1\text{Ori C}$ . In configuration (a) the proplyds are roughly side-by-side as seen from  $\theta^1\text{Ori C}$ , with the stagnation point forming between them. Whereas in configuration (b), the smaller proplyd is closer to  $\theta^1\text{Ori C}$ , resulting in the tail flow from this smaller proplyd interacting with the head flow from the larger proplyd, with the stagnation point forming close to the base of the smaller proplyd’s tail, as suggested in § 3. In both cases the stagnation point will be seen to lie between the proplyds, but in configuration (a) it will be superimposed on the tail of 168–326NW. This superposition can be seen in the *HST* image in Figure 5 and therefore favours the side-by-side configuration. However, this configuration places the observer within the ‘bowshock cone’, implying that an arc would not be observed. The observed arc in the *HST* images favours configuration (b). If the observer does lie outside the bowshock cone, then the shell would be seen tangentially at some point and the fact that it is clearly resolved with the *HST* would put a lower limit on its thickness.

In order to conclusively choose between these two configurations, the morphological appearance of the shell has been modelled for both cases. For this, a model for the shape of the shell was needed, and has been provided by the CRW model. The shape of a CRW shell is characterised by its asymptotic opening angle,  $\theta_\infty$ , which is uniquely determined by the momentum flux ratio,  $\beta$ , of the two interacting flows. In Figure 8, this shape for  $\beta = 5$ ,  $\theta_\infty = 61.9^\circ$  has been used to calculate the appearance of a shell at various viewing angles,  $\alpha$ , the angle between the line of sight and the bowshock axis for a cylindrically symmetric bowshock. It can be seen that the morphology of the modelled shell when viewed from within the bowshock cone with  $\alpha = 61^\circ$  is close to that of the observed shell, but this modelled shell has no apparent curvature. In fact, the observed curvature is similar to a modelled shell with  $\alpha = 63^\circ$ , with the observer outside the bowshock cone. This discrepancy could be explained by the fact that the bowshock need not be cylindrically symmetric. Each proplyd has a distinctive cometary shape extending away from  $\theta^1\text{Ori C}$  along an axis referred to as the proplyd axis (see Figure 7). If there is a contribution to a proplyd’s flow from the entire length of the proplyd axis, the bowshock between two proplyds is likely to be flattened in the direction perpendicular to the proplyd axis. The appearance of an asymmetric bowshock can be modelled by arbitrarily decreasing  $\beta$  and therefore increasing  $\theta_\infty$  in the direction

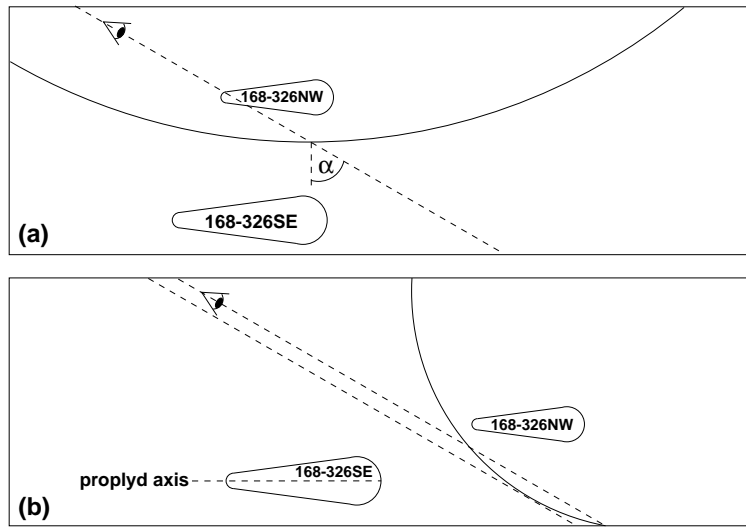


Fig. 7.— Two possible geometrical configurations for the LV 1 binary system. (a): Side-by-side configuration. (b): Head-tail configuration. The observer's line of sight through the stagnation point of the shell is indicated by a dashed line (in reality the line of sight is slightly inclined with respect to the plane of the diagram). In configuration (a), the angle between the line of sight and the bowshock axis,  $\alpha$ , is defined. In configuration (b), the lower dashed line indicates the line of sight that is tangent to the shell and the proplyd axis is defined.

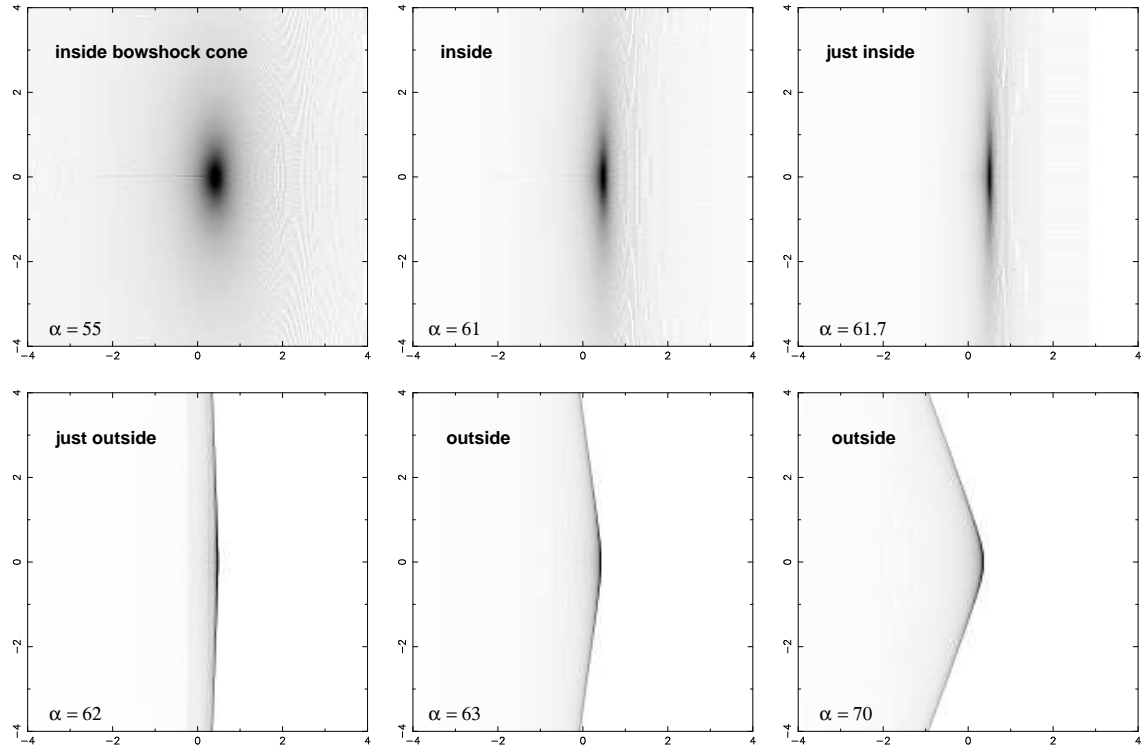


Fig. 8.— Modelled images of a cylindrically symmetric CRW shell for an asymptotic opening angle,  $\theta_\infty = 61.9^\circ$  and a wind momentum flux ratio,  $\beta = 5$  at various viewing angles,  $\alpha$ . Whether the observer is inside or outside the bowshock cone is indicated. The greyscale intensity in each panel is normalized to the maximum pixel of the image.

parallel to the proplyd axis. This will result in a bowshock whose cross-section resembles an ellipse with a major axis parallel to the proplyd axis. Figure 9 is a set of modelled images for such an asymmetric bowshock, with the  $\theta_\infty$  increased to  $75^\circ$  in the direction parallel to the proplyd axis. With  $\alpha = 0$  the intrinsic flatness of the bowshock can be seen, giving rise to elliptical isophotes with a major axis in the horizontal direction. As  $\alpha$  increases this horizontal elongation decreases and at  $\alpha \approx 45^\circ$ , the intrinsic elongation has been cancelled out, giving rise to approximately circular isophotes. As  $\alpha$  continues to increase the apparent elongation is in the vertical direction and some apparent curvature is visible along the bowshock, even with the observer still inside the bowshock cone. With  $\alpha = 70^\circ$ , the morphology of the modelled image is a good match for the observed morphology, in terms of both smoothness and curvature (see Figures 4 & 5). In these modelled images (Figures 8 & 9), the thickness of the shell has been assumed to be unresolved, as can be seen in those images where the shell is viewed tangentially. Henney (2001) predicts that the shell's thickness is likely to be unresolved with the *HST*. However, the presence of a magnetic field in the shell will act as an additional pressure, which will thicken the interproplyd shell. If this magnetic pressure dominates the thermal pressure in holding the shell up against the ram pressure of the two incident flows, the density in the region will be lower than that predicted by Henney (2001). A lower density will lower the cooling rate and cause the cooling length to increase. Therefore a significant magnetic field increases both the overall size of the shell and the cooling length within it. If this effect is large enough, the shell could be viewed from outside the bowshock cone, and therefore tangentially, and still be resolved. Dust (other than foreground extinction from the neutral veil) will be unimportant because the column density of the shocked shell is too low.

## 5. Nature of the Radio Emission

An interaction zone between the two components of the binary proplyd, LV 1, has been detected in both the radio and optical domains. This appears as an extended arc, containing a compact (5 GHz) knot. The morphology of the interacting proplyd binary is similar to that of other interacting binaries such as WR 147 (see e.g. Williams et al. 1997; Niemela et al. 1998). In such cases the interaction radio source is non-thermal, synchrotron emission caused by shock-accelerated, relativistic electrons. High energy electrons can be produced in this scenario, because at least one of the winds has a speed of order  $1000 \text{ km s}^{-1}$ . In the case of the proplyds, the speed of the evaporated flows is thought to be a few times the sound speed of  $10 \text{ km s}^{-1}$  and the bulk of the emission from LV 1 appears to be from gas flowing at velocities of less than  $50 \text{ km s}^{-1}$  (Figure 2). Two interacting flows each with this velocity, would lead to two shocked layers at a post-shock temperature of  $\approx 3 \times 10^4 \text{ K}$  (Dyson &

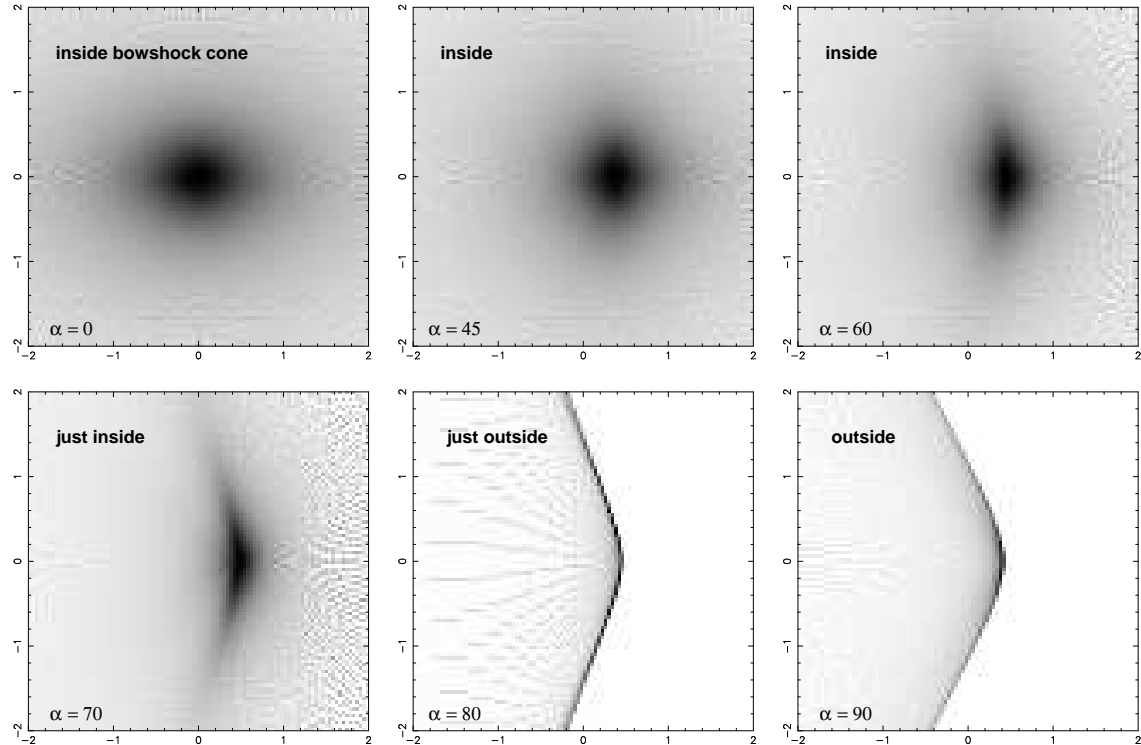


Fig. 9.— Modelled images of an asymmetric CRW shell for orthogonal asymptotic opening angles,  $\theta_\infty = 75^\circ$ ,  $62^\circ$  and orthogonal wind momentum flux ratios,  $\beta = 2, 5$  at various viewing angles,  $\alpha$ . Whether the observer is inside or outside the bowshock cone is indicated. The greyscale intensity in each panel is normalized to the maximum pixel of the image.

Williams 1997). Although this is high enough to explain the enhanced [OIII] emission from the interaction region, it is not sufficient to account for the existence of relativistic electrons. Therefore, synchrotron emission is not expected from these low speed collisions.

The 5 GHz radio/H $\alpha$  intensity ratio is approximately 2.6 times higher for the interaction region than for the proplyds. For identical physical conditions in the proplyds and the interaction region, this could be indicative of non-thermal radio emission from the interaction zone. However, it has already been established that the post-shock material in this zone is likely to have a higher temperature than the proplyds. Post-shock material is also unlikely to have the same density as the unshocked material flowing from the proplyd. The canonical density jump for a strong shock is a factor of 4 (Dyson & Williams 1997), but for weaker shocks this factor is lower. Once the post-shock material has cooled, the final compression ratio as compared with preshocked material will be higher than this. It should also be noted that the material is flowing from the proplyd down a density,  $N$ , gradient that, for an accelerating spherical flow, would scale with radial distance from the centre of the proplyd disk,  $r$ , as follows,

$$N(r) = N(r_{\text{if}}) \left( \frac{r_{\text{if}}}{r} \right)^2 \left( \frac{V_{\text{if}}}{V(r)} \right) \quad (1)$$

where  $r_{\text{if}}$  is the radius of the proplyd ionization front (IF),  $N(r_{\text{if}})$  is the density at this radius,  $V_{\text{if}}$  is the gas velocity at the IF ( $\approx$  sound speed) and  $V(r)$  is the gas velocity. The interaction between 168–326SE and 168–326NW is happening at approximately 2–3 IF radii. Therefore, in the case of a spherical flow from the proplyds, a density drop of a factor of  $> 4$  would be expected in the pre-shocked proplyd flow as compared with material flowing from the IF. As a result, even after compression due to the shock, the density in the post-shock material in the interproplyd shell is likely to be lower than the density at the proplyd's IF. This difference in both temperature and density between the IF and the interproplyd shell could provide an explanation for the observed difference in 5 GHz radio/H $\alpha$  intensity ratio. However, the contribution from the high temperature gas, which will rapidly cool through [OIII] emission, depends on its cooling length as compared with the total length of the interproplyd shell. If this contribution from the post-shock cooling layer is insignificant, the majority of the material in the shell will be at the equilibrium nebular temperature of 10<sup>4</sup> K. The density of this cooled material will be higher than that in the cooling layer, but still different to that at the proplyd IF.

Using the tabulated values of  $j_{\text{H}\alpha}$ , the emission coefficient of the H $\alpha$  line provided by Storey & Hummer (1995) at various temperatures,  $T$ , the H $\alpha$  flux density from an object with uniform density,  $N$ , at a distance,  $D$ , for case B recombination is

$$F(\text{H}\alpha) = 1.850 \times 10^{-21} T^{-0.932} N^2 R^3 D^{-2} \text{ (erg cm}^{-2} \text{ s}^{-1}\text{)}, \quad (2)$$

where  $R$  is the radius of the object. Using typical values for the proplyds, equation (2) predicts flux densities of order  $10^{-11}$  erg cm $^{-2}$  s $^{-1}$ , which is consistent with the total fluxes calculated by O'Dell (1998).

The radio flux,  $S_\nu$ , due to thermal brehmstrahlung from a source observed at a frequency,  $\nu$ , is

$$S_\nu = \frac{2k\nu^2\Omega}{c^2} T (1 - e^{-\tau_\nu}), \quad (3)$$

where  $\Omega$  is the solid angle of the source and  $\tau_\nu$  is the optical depth. This is reasonably approximated by the following relationship

$$\tau_\nu = 8.235 \times 10^{-2} \left( \frac{T}{K} \right)^{-1.35} \left( \frac{\nu}{\text{GHz}} \right)^{-2.1} \left( \frac{EM}{\text{pc cm}^{-6}} \right) \quad (4)$$

where  $EM \approx N^2 R$  is the emission measure (Mezger & Henderson 1967). For typical values for the proplyds at 5 GHz, this is close to 1, so the proplyds can neither be treated as optically thin nor thick at this frequency. A full treatment allowing for an arbitrary optical depth is required.

Therefore, the peak H $\alpha$  flux ratio for two objects at temperatures,  $T_1$  and  $T_2$ , densities,  $N_1$  and  $N_2$  and sizes  $R_1$  and  $R_2$  is given by

$$\frac{F(\text{H}\alpha)_1}{F(\text{H}\alpha)_2} = \left( \frac{T_1}{T_2} \right)^{-0.932} \left( \frac{N_1}{N_2} \right)^2 \left( \frac{R_1}{R_2} \right) \quad (5)$$

and the 5 GHz radio flux ratio for the two objects with optical depths,  $\tau_{5\text{GHz}(1)}$  and  $\tau_{5\text{GHz}(2)}$  is given by

$$\frac{S_{5\text{GHz}(1)}}{S_{5\text{GHz}(2)}} = \frac{T_1 (1 - e^{-\tau_{5\text{GHz}(1)}})}{T_2 (1 - e^{-\tau_{5\text{GHz}(2)}})}. \quad (6)$$

These ratios are known for 168–326SE compared to the interaction zone from the *HST* and MERLIN 5 GHz data, to be 3.4 in H $\alpha$  and 1.3 in the radio. Equations (5) and (6) can be solved simultaneously for  $T_2$  and  $N_2$ , given values for  $T_1$  and  $N_1$ , i.e. given a temperature and density for 168–326SE a temperature and density consistent with the flux ratios can be found for the interaction zone. A scale-size is needed in order to estimate the volume of material being observed. For both the proplyd and the interaction zone, this was chosen to be  $10^{-4}$  pc ( $\equiv 20$  AU), which is approximately the radius of the IF for a proplyd. With  $T_1 = 10^4$  K and  $N_1 = 10^6$  cm $^{-3}$  for the proplyd, the equations are solved with  $T_2 = 25470$  K and  $N_2 = 0.839 \times 10^6$  cm $^{-3}$  for the interaction zone. These values are consistent with both the temperature predicted by the shock speed and the expectation that the density should be lower in the interaction zone. However, the values are sensitive to the chosen scale-size, initial temperature ( $T_1$ ) and density ( $N_1$ ). The H $\alpha$  fluxes could also be significantly affected

by extinction. Nevertheless, this treatment shows that by changing the temperature and density in the post-shock region, the required flux ratios can be arrived at without the need for a non-thermal source of radio emission, as long as there is sufficient material at the high post-shock temperature and lower density. If there is insufficient post-shock material, as suggested by Henney (2001), the difference in density between the proplyd and the cooled material could still explain the difference in 5 GHz radio/H $\alpha$  intensity ratio between the two regions. The intensity ratio is also affected by the physical size of the emitting region, so the uncertainty in the shell thickness and cooling length makes it difficult to determine whether the radio emission has a thermal origin.

The spectral index of the interaction compact radio source is now needed to distinguish conclusively between a thermal or non-thermal origin. For this, observations are needed at 1.5 GHz (20 cm) with a similar angular resolution to that of the 5 GHz MERLIN observations presented here.

## 6. Conclusions

The Orion proplyd originally designated LV 1 is shown at both radio (with MERLIN) and optical wavelengths (with the HST) to be a proplyd binary system with an interaction zone separating the two components 168-326NW and 168-326SE.

Comparison of detailed hydrodynamical modelling of the interaction zone with the observations has identified the geometry of the system convincingly.

A strong 6 cm radio source coincides with the stagnation point in this interaction zone. The present observations cannot distinguish between a thermal or non-thermal origin for this radio emission. Observations at 20 cm but with a similar angular resolution (0.1 '') are awaited to clarify this point through measurement of the radio spectral index.

The existence of a high-speed micro-jet from the binary component 168-326SE is also suggested by spectral observations and HST imagery.

## Acknowledgements

MFG would like to acknowledge a studentship received from the Particle Physics and Astronomy Research Council (PPARC). MERLIN is a national facility operated by the University of Manchester on behalf of PPARC in the U.K. The work presented in this paper is based on observations made with MERLIN and the NASA/ESA Hubble Space Telescope,

the latter obtained from the data archive at the Space Telescope Science Institute. STScI is operated by the Association of Universities for Research in Astronomy, Inc. under NASA contract NAS 5-26555.

## REFERENCES

Bally, J., Sutherland, R. S., Devine, D., & Johnstone, D. 1998, AJ, 116, 293

Bally, J., O'Dell, C. R., & McCaughrean, M. J. 2000, AJ, 119, 2919

Canto, J., Raga, A. C., & Wilkin, F. P. 1996, ApJ, 469, 729 (CRW)

Churchwell, E., Felli, M., Wood, D. O. S., & Massi, M. 1987, ApJ, 321, 516

Dyson, J. E. 1968, Ap&SS, 1, 388

Dyson, J. E. & Williams, D. A. 1997, The physics of the interstellar medium. Edition: 2nd ed. Publisher: Bristol: Institute of Physics Publishing, 1997. Edited by J. E. Dyson and D. A. Williams. Series: The graduate series in astronomy. ISBN: 0750303069,

Felli, M., Churchwell, E., Wilson, T. L., & Taylor, G. B. 1993a, A&AS, 98, 137

Felli, M., Taylor, G. B., Catarzi, M., Churchwell, E., & Kurtz, S. 1993b, A&AS, 101, 127

Garay, G., Moran, J. M., & Reid, M. J. 1987, ApJ 314, 535

Garay, G. 1987, RevMexAA, 14, 489

García-Arredondo, Henney, & Arthur 2001, ApJ, 561,

Hayward, T. L., Houck, J. R., & Miles, J. W. 1994, ApJ, 433, 157

Henney, W. J., Raga, A. C., Lizano, S., & Curiel, S. 1996, ApJ, 465, 216

Henney, W. J., Meaburn, J., Raga, A. C., & Massey, R. 1997, A&A, 324, 656

Henney, W. J. & Arthur, S. J. 1998, AJ, 116, 322

Henney, W. J. & O'Dell, C. R. 1999, AJ, 118, 2350

Henney, W. J., O'Dell, C. R., Meaburn, J., Garrington S. T. & López J. A., 2001, ApJ, in press.

Henney, W. J., 2001, Rev. Mexicana Astron. Astrofis., in preparation

Johnstone, D., Hollenbach, D., & Bally, J. 1998, *ApJ*, 499, 758

Laques, P. & Vidal, J. L. 1979, *A&A*, 73, 97

Massey, R. M. & Meaburn, J. 1993, *MNRAS*, 262, L48

Massey, R. M. & Meaburn, J. 1995, *MNRAS*, 273, 615

McCaughrean, M. J. & Stauffer, J. R. 1994, *AJ*, 108, 1382

McCullough, P. R., Fugate, R. Q., Christou, J. C., Ellerbroek, B. L., Higgins, C. H., Spinhirne, J. M., Cleis, R. A., & Moroney, J. F. 1995, *ApJ*, 438, 394

Meaburn, J. 1988, *MNRAS*, 233, 791

Meaburn J., Blundell B., Carling R., Gregory D. F., Keir D., & Wynne C. G. 1984, *MNRAS*, 210, 463

Meaburn, J., Massey, R. M., Raga, A. C., & Clayton, C.A. 1993, *MNRAS*, 260, 625

Mezger, P. G. & Henderson, A. P. 1967, *ApJ*, 147, 471

Niemela, V. S., Shara, M. M., Wallace, D. J., Zurek, D. R., & Moffat, A. F. J. 1998, *AJ*, 115, 2047

O'Dell, C. R., Wen, Z., & Hu, X. 1993, *ApJ*, 410, 696

O'Dell, C. R. & Wen, Z. 1994, *ApJ*, 436, 194

O'Dell, C. R. 1998, *AJ*, 115, 263

O'Dell, C. R. & Wong, S. K. 1996, *AJ*, 111, 846

O'Dell, C. R., Hartigan, P., Bally, J., & Morse, J. A. 1997, *AJ*, 114, 2016

O'Dell, C. R. & Doi, T. 1999, *PASP*, 111, 1316

Petr, M. G., Coude Du Foresto, V., Beckwith, S. V. W., Richichi, A., & McCaughrean, M. J. 1998, *ApJ*, 500, 825

Storey, P. J. & Hummer, D. G. 1995, *MNRAS*, 272, 41

Störzer, H. & Hollenbach, D. 1999, *ApJ*, 515, 669

Williams, P. M., Dougherty, S. M., Davis, R. J., van der Hucht, K. A., Bode, M. F., & Setia Gunawan, D. Y. A. 1997, *MNRAS*, 289, 10

